Nonlinear regime of a multimode Richtmyer–Meshkov instability: A simplified perturbation theory

Marc Vandenboomgaerde, Serge Gauthier, and Claude Mügler

Citation: Phys. Fluids **14**, 1111 (2002); doi: 10.1063/1.1447914
View online: http://dx.doi.org/10.1063/1.1447914
View Table of Contents: http://pof.aip.org/resource/1/PHFLE6/v14/i3
Published by the American Institute of Physics.

Nonlinear regime of a multimode Richtmyer–Meshkov instability: A simplified perturbation theory

Marc Vandenboomgaerde, Serge Gauthier, and Claude Mügler
Commissariat à l'Energie Atomique, Bruyères-Le-Châtel, Boite Postale 12, 91680 Bruyères-Le-Châtel, France

(Received 30 May 2001; accepted 11 December 2001)

In this paper we present a drastic simplification of the perturbation method for the Richtmyer–Meshkov instability developed by Zhang and Sohn [Phys. Fluids **9**, 1106 (1997)]. This theory is devoted to the calculus of the growth rate of the perturbation of the interface in the weakly nonlinear stage. In the standard approach, expansions appear to be power series in time. We build accurate approximations by retaining only the terms with the highest power in time. This simplifies and accelerates the solution. High-order expressions are then easily reachable. Furthermore, computations for multimode interfaces become tractable. The accuracy of this approach is checked against two-dimensional numerical simulations. The selection mode process is studied and the phase between modes is shown to be as important as the wave number or the amplitude. Inferences for the intermediate nonlinear regime are also proposed. In particular, a class of homothetic configurations is inferred; its validity is verified with numerical simulations even as vortex structures appear at the interface. © *2002 American Institute of Physics.* [DOI: 10.1063/1.1447914]

I. INTRODUCTION

When the interface between two materials of different densities is not perfectly flat and is accelerated by a shock wave, it can become unstable. This interface instability is known as the Richtmyer–Meshkov (RM) instability from the authors of the first theoretical[1] and experimental[2] studies. This instability is involved in several physical phenomena. For example, it may provide some explanations of supernovas behavior. It can also decrease the gain of inertial confinement fusion (ICF) targets by breaking the sphericity of the implosion. Indeed, if no particular care is taken, and since its manufacturing is not perfect, the interface is usually perturbed. Its shape is a combination of numerous modes with different amplitudes. The same phenomenon arises in shock tube experiments. After the shock passage through the interface, the various modes of the perturbation first grow linearly and independently. Afterward, harmonics appear and, little by little, influence the growth of other modes. After this early nonlinear stage, the competition between modes may become more important. In time, the emerging modes turn into complex structures and the interface becomes mushroom shaped. Dominant modes can still be identified in this intermediate nonlinear stage. Then, the flow develops into a disordered state; this highly nonlinear regime can be considered as a preturbulent stage.

Several theoretical works have described the linear stage of the RM instability.[1,3–8] Perturbation methods[9] have been used by several authors to describe the weakly nonlinear regime of interfacial instabilities.[10–14] In particular, the first step has been carried out by Ingraham for the Rayleigh–Taylor instability. In such methods, the small parameter is the initial wave steepness, $a_0 k$, where a_0 and k are the initial amplitude and the wave number of the interface, respectively. On the other hand, the advanced nonlinear stage may be handled by bubble evolution models.[15,16]

The basis of this paper is the recent application of the perturbation expansions performed by Zhang and Sohn[12] for the weakly nonlinear stage of the RM instability. Hereafter, we shall refer to this work as the full perturbation theory. In this paper, we present a way to drastically simplify and accelerate the calculus by retaining the most secular term at each order.[9,17] This new approach makes perturbation expansions for multimode configurations easily reachable and tractable even at high order. Furthermore, the simplicity of the writing has brought out some features of the nonlinear evolution of the RM instability; they were previously hidden by the complexity of the results or the restriction to specific values of the Atwood number. It will be shown by comparing these results with two-dimensional (2-D) numerical simulations, that these features that have been derived within the framework of the weakly nonlinear theory hold for the intermediate nonlinear stage.

The paper is organized as follows. In Sec. II, we detail the perturbation theory for a single-mode interface. First, the full perturbation theory is summarized and its range of validity is discussed. Then, we present a simplification of this method. Finally, comparisons with 2-D simulations confirm the accuracy of the theory. In Sec. III, this approach is generalized to multimode interaction. Theoretical and computational results of mode competitions are compared. In Sec. IV, we propose some inferences derived from the present weakly nonlinear theory. Simulations show that these conclusions seem to remain valid at a later time, in the intermediate nonlinear regime.

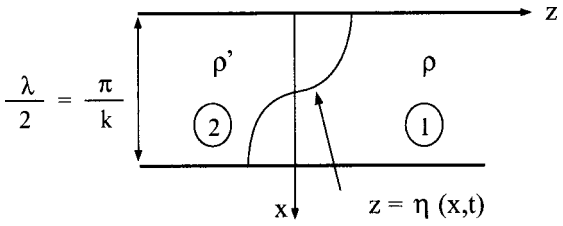

FIG. 1. Sketch of the configuration.

II. PERTURBATION EXPANSIONS FOR SINGLE-MODE CONFIGURATIONS

A. Summary of the full perturbation theory (Ref. 12)

One considers two different fluids separated by a sine-shape interface that is described by $z=\eta(x,t)$. At time $t=0$, this shape is written as $z=a_0\cos kx$. A shock wave comes from positive z and passes through the interface. The flow is inviscid, irrotational, and incompressible. As a result, the reflected and transmitted waves no longer influence the interface. For consistency and matching between theories, the amplitude of $\dot{\eta}(x,0)$ can be put equal to the asymptotic velocity that is obtained from the compressible linear theory. A sketch of the interface is presented in Fig. 1. The equations are written in the frame of the unperturbed interface; this is a Galilean frame. The velocity potentials are $\Phi(x,z,t)$ and $\Phi'(x,z,t)$ for the fluids 1 and 2, respectively. They satisfy the following equations:

$$\Delta\Phi(x,z,t)=0 \quad \text{in fluid 1,} \tag{1}$$

$$\Delta\Phi'(x,z,t)=0 \quad \text{in fluid 2.} \tag{2}$$

The matching conditions at the interface are given by the motion equations and the Bernoulli's equation,

$$\frac{\partial\eta}{\partial t}-\frac{\partial\Phi}{\partial x}\frac{\partial\eta}{\partial x}+\frac{\partial\Phi}{\partial z}=0 \quad \text{at } z=\eta, \tag{3}$$

$$\frac{\partial\eta}{\partial t}-\frac{\partial\Phi'}{\partial x}\frac{\partial\eta}{\partial x}+\frac{\partial\Phi'}{\partial z}=0 \quad \text{at } z=\eta, \tag{4}$$

$$-\rho'\frac{\partial\Phi'}{\partial t}+\rho\frac{\partial\Phi}{\partial t}+\frac{1}{2}\rho'\left[\left(\frac{\partial\Phi'}{\partial x}\right)^2+\left(\frac{\partial\Phi'}{\partial z}\right)^2\right]-\frac{1}{2}\rho\left[\left(\frac{\partial\Phi}{\partial x}\right)^2+\left(\frac{\partial\Phi}{\partial z}\right)^2\right]=0 \quad \text{at } z=\eta. \tag{5}$$

The boundary conditions are $\Phi(x,+\infty,t)=0$ and $\Phi'(x,-\infty,t)=0$. The initial conditions are $\eta(x,0)=a_0\cos kx$ and $\dot{\eta}(x,0)=a_0\sigma\cos kx$, where σ is a constant.

In order to derive a perturbation method, each quantity is expanded as a series of powers of a small parameter. This parameter is classically the initial wave steepness a_0k. By doing so, the interface shape and velocity potentials are written as

$$\eta(x,t)=\sum_{n=1}^{+\infty}\eta^{(n)}(x,t), \quad \Phi(x,z,t)=\sum_{n=0}^{+\infty}\Phi^{(n)}(x,z,t),$$

$$\Phi'(x,z,t)=\sum_{n=0}^{+\infty}\Phi'^{(n)}(x,z,t). \tag{6}$$

The nth term of the series (6) is of the order of $(a_0k)^n$. In order to simultaneously solve Eqs. (3)–(5), terms in series (6) are further expanded:

$$\eta^{(n)}(x,t)=\sum_{1\leqslant j\leqslant n}a_j^{(n)}(t)\cos jkx,$$

$$\Phi^{(n)}(x,z,t)=\sum_{0\leqslant j\leqslant n}b_j^{(n)}(t)\cos jkxe^{-jkz}, \tag{7}$$

$$\Phi'^{(n)}(x,z,t)=\sum_{0\leqslant j\leqslant n}b_j'^{(n)}(t)\cos jkxe^{+jkz}.$$

At the nth order, the terms of the order of $(a_0k)^n$ are collected and the resulting equations are projected on the cosine base $\{\cos jkx, 0\leqslant j\leqslant n\}$. This leads to $(n+1)$ systems of three differential equations that involve derivatives of the quantities $a_j^{(n)}(t)$, $b_j^{(n)}(t)$, and $b_j'^{(n)}(t)$ with respect to time. They are easily solved by integration. The unknowns are found to be polynomials of the nth degree. At the nth order, $3(n+1)$ integrations are needed in order to evaluate the $(n+1)$ coefficients of each polynomial. So, $3(n+1)^2$ coefficients must be computed and stored.

The results up to the third order are[12]

$$\eta^{(1)}(x,t)=(a_0+a_0\sigma t)\cos kx,$$

$$\eta^{(2)}(x,t)=\tfrac{1}{2}a_0^2k\sigma^2At^2\cos 2kx, \tag{8}$$

$$\eta^{(3)}(x,t)=-\tfrac{1}{24}k^2a_0^3\sigma[(4A^2+1)\sigma^2t^3+3\sigma t^2+6t]\times\cos kx+\tfrac{1}{8}k^2a_0^3\sigma[(4A^2-1)\sigma^2t^3-3\sigma t^2]\cos 3kx,$$

where A is the post-shocked Atwood number; $A=(\rho'-\rho)/(\rho'+\rho)$. The amplitude of the interface is defined as

$$a(t)=\frac{1}{2}\left[\eta(0,t)-\eta\left(\frac{\pi}{k},t\right)\right]. \tag{9}$$

Let us remark that the set of Eqs. (3)–(5) does not provide a value of σ. However, there are several ways to determine this value. First, the impulsive model may be used.[1,18,19] It has been shown that this model is valid for low Mach numbers and not too different adiabatic coefficients.[5,19] The value of σ is then given by the following expression:[19]

$$\sigma=\frac{1}{2}k\Delta U\left(A+\frac{A^-}{1-\dfrac{\Delta U}{W_i}}\right), \tag{10}$$

where ΔU, W_i, and A^- are the velocities of the shocked interface, the incident shock wave and the pre-shocked Atwood number, respectively. Second, 2-D simulations can be run in order to calculate the amplitude $a(t)$. The value of σ is then estimated by $\dot{a}(0^+)$. Third, σ can be given by the asymptotic growth rate obtained with any linear theory[1,4–8] based on the full Euler's equations, i.e., taking into account the compressibility. Indeed, such theories provide a constant asymptotic growth rate. In this paper, σ is usually computed in this way.

B. How to simplify the full perturbation theory

Recall that all physical quantities have been expanded as a series of power of the small parameter, a_0k. On the other hand, results to the third order, Eqs. (8), show that time appears explicitly in the coefficients. Then, such a series can be considered as a series in the power of time. It is remarkable that, at the order n, the leading term, i.e., the term with the highest power of time, is written as $(a_0k\sigma t)^n\alpha_n$, where α_n is a polynomial of the Atwood number A and the function $\cos kx$. The quantity $a_0k\sigma t$ is the product of the small parameter, a_0k, with the scaled time, σt.

It is well known that in such perturbation expansions, an accurate approximation can usually be built with only the most secular terms (see, for example, Ref. 17). The most secular term is defined as the term with the highest unbounded part. For example, retaining only the terms with the highest power in time in the full perturbation theory, Eqs. (8), gives

$$\eta^{(1)}(x,t)\approx a_0\sigma t\cos kx,$$

$$\eta^{(2)}(x,t)=\tfrac{1}{2}a_0^2k\sigma^2At^2\cos 2kx,$$

$$\eta^{(3)}(x,t)\approx k^2a_0^3\sigma^3t^3\left(-\tfrac{1}{24}(4A^2+1)\cos kx+\tfrac{1}{8}(4A^2-1)\cos 3kx\right).$$

This approximation gives an accurate time evolution provided the time is large enough. Discrepancies may occur near the origin $t=0$. Fortunately, for the RM instability, the approximate first- and second-order growth rates are identical to those of the complete theory. So, it turns out that the approximation is also accurate near $t=0$. In order to get an expression valid at $t=0$, we have to add the constant term a_0. In the following expressions, we shall replace the symbol $\approx$ by $=$.

C. Derivation of the approximate perturbation theory

As already stated, in order to build an approximate theory, the terms with the highest power in time must be retained. By inspection of the results of the full perturbation theory,[12] up to the fourth order, we put as general forms for the most secular part of $\eta^{(n)}$, $\Phi^{(n)}$, and $\Phi'^{(n)}$, the following expressions:

$$k\eta^{(n)}=(a_0k\sigma t)^n\sum_{j=1}^{n}a_j^{(n)}\cos jkx,$$

$$\frac{k^2}{\sigma}\Phi^{(n)}=(a_0k)^n(\sigma t)^{n-1}\sum_{j=0}^{n}b_j^{(n)}\cos jkxe^{-jkz},\qquad(11)$$

$$\frac{k^2}{\sigma}\Phi'^{(n)}=(a_0k)^n(\sigma t)^{n-1}\sum_{j=0}^{n}b_j'^{(n)}\cos jkxe^{+jkz}.$$

The unknowns $(a_j^{(n)},b_j^{(n)},b_j'^{(n)})$ are now real numbers. If the scaled time is of order of $(a_0k)^{-1}$ $(\sigma t=O[(a_0k)^{-1}])$, second terms of the series (6) are of the same order of the first terms, contrary to our assumption that, for example, $\eta^{(2)}$ is a small correction of $\eta^{(1)}$ (see Ref. 9, p. 25). The series (6) are only valid for $0\leqslant t\leqslant t_{vs}$, where t_{vs} is some finite period not very large compared to $(a_0k\sigma)^{-1}$ (see Ref. 20, p. 107). One can see graphically by plotting series given by (6) up to the 11th order versus $a_0k\sigma t$, and for all Atwood numbers, that they diverge for $a_0k\sigma t=1$. So, we shall use $t_{vs}=(a_0k\sigma)^{-1}$.

In Eqs. (3)–(5), the classical theory leads to some complicated selection rule in order to select the terms of a given order [see Eqs. (16)–(18) in Ref. 12]. Using only the most secular term brings strong simplification. Indeed, the selection is straightforward. At the nth order, the position of the interface, $\eta(x,t)$, is of order of t^n. So, the most secular terms of Eqs. (3) and (4) are proportional to $(a_0k\sigma t)^{n-1}$. This is due to the first derivative of $\eta(x,t)$ with respect to time. So, at the nth order, the terms to be kept are the quantities that give a t^{n-1} dependence. The same argument is applied to Eq. (5). The time dependence of the most secular terms in this equation is t^{n-2}, as only the first derivatives with respect to the time of Φ and Φ' are involved. Keeping only these terms, a system of the following form is obtained:

$$\begin{aligned}&B(a_j^{(n)},b_j^{(n)},b_j'^{(n)},\cos jkx)_{0\leqslant j\leqslant n}=0,\\&C(a_j^{(n)},b_j^{(n)},b_j'^{(n)},\cos jkx)_{0\leqslant j\leqslant n}=0,\\&D(a_j^{(n)},b_j^{(n)},b_j'^{(n)},\cos jkx)_{0\leqslant j\leqslant n}=0,\end{aligned}\qquad(12)$$

where B, C and D are combinations of the unknowns $(a_j^{(n)},b_j^{(n)},b_j'^{(n)})_{0\leqslant j\leqslant n}$ and the functions $(\cos jkx)_{0\leqslant j\leqslant n}$. Let us emphasize that keeping only the most secular terms allows us to cancel the time dependence in the system (12). The projection of this system on the Fourier cosine orthogonal system leads to $(n+1)$ systems of three equations with three real unknowns, at the nth order. They are written as

$$\begin{aligned}&B_i'(a_j^{(n)},b_j^{(n)},b_j'^{(n)})=0,\\&C_i'(a_j^{(n)},b_j^{(n)},b_j'^{(n)})=0,\quad\text{for } 0\leqslant i\leqslant n,\\&D_i'(a_j^{(n)},b_j^{(n)},b_j'^{(n)})=0,\end{aligned}\qquad(13)$$

where B_i', C_i', and D_i' are combinations of the unknowns $(a_j^{(n)},b_j^{(n)},b_j'^{(n)})_{0\leqslant j\leqslant n}$. Since the systems (13) are algebraic, they do not require time integration anymore. The $3(n+1)$ coefficients of expressions (11) are simply obtained through $3(n+1)$ algebraic solutions. Let us emphasize that the standard theory requires $3(n+1)$ time integrations in order to calculate $3(n+1)^2$ coefficients.

We now summarize the solution method.

(i) Every quantity is expanded as a series of powers of the small parameter $a_0k\sigma t$. This leads to expressions (11) for $\eta^{(n)}$, $\Phi^{(n)}$, and $\Phi'^{(n)}$.

(ii) At the nth order, terms of order of t^{n-1} are retained in the expansions of the boundary conditions, Eqs. (3) and (4). Terms of order of t^{n-2} are kept in the expression of the Bernoulli's equation (5).

(iii) By using the orthogonality of the Fourier functions, algebraic systems are obtained.

The above procedure is very easily handled by symbolic computation softwares. The approximate approach brings the following advantages compared with the classical perturbation method.

(a) A simpler writing of the unknowns: one deals with real numbers instead of polynomials.
(b) An easier solution and identification of terms of the same order: the knowledge of the time exponent is only needed.
(c) A faster solution as no time integration is needed; only $3(n+1)$ coefficients are computed instead of $3(n+1)^2$.
(d) A smaller storage space for the results is necessary.

D. Numerical applications: Quantitative results

The values of the $a_j^{(i)}$ up to the seventh order are given in Appendix A. It can be verified for the first four orders that the approximate theory gives the terms with the highest power in time of the full perturbation theory.[12] We have also checked that the $a_n^{(n)}$ $(1 \leqslant n \leqslant 11)$ obtained from the approximate perturbation theory are the same as those of Eq. (6) derived by Velikovich and Dimonte[14] for $A=1$. Note that this equation is an analytic formula. For orders higher than 4 and an arbitrary Atwood number, no result is available from the full perturbation theory. As noticed by Zhang and Sohn in Ref. 13, "*at this order [4th], the expansion is rather complicated and inclusion of higher order terms is avoided.*"

From our results, it can be seen that the growth of the amplitude of odd harmonics, i.e., modes the wave number of which is written as $(2p+1)k$, where p is an integer, is an odd function of a_0; on the other hand, the growth of the amplitude of even harmonics is an even function of a_0. So, whatever the sign of a_0, the even harmonics have a positive amplitude.

In order to test the accuracy of the approximate theory, we have computed the growth of a single-mode interface. This is done by numerical simulation with the 2-D CADMÉE code.[21] In our simulations, the two fluids are considered inviscid and nondiffusive. Their mixing is described within the single fluid approximation by a concentration (c) governed by an advection equation. In order to compute the growth of each mode, a Fourier analysis of the isoconcentration curve $c=0.5$ is performed.

The values of the physical parameters are taken from Benjamin's experiments.[22] In these experiments, a 1.24 Mach number shock wave moves from air to SF_6. The initial pressure of gases is 0.8×10^5 Pa. The post-shocked Atwood number is 0.706. The wave number and the initial preshocked amplitude of the perturbation are $k=130\,\mathrm{m}^{-1}$ and $a_0^- = +0.72\times10^{-3}$ m, respectively. For these experiments, the asymptotic growth rate given by the linear theory[5] is $\dot{a}(t)=0.113ka_0^-W_i$. These values lead to a parameter σ equal to 7451 s^{-1}. The value of t_{vs} for this configuration is $t_{vs}=1.77\times10^{-3}$ s. The numerical simulations utilize 180 nodes in order to describe this wavelength and 30 nodes for this peak-to-valley amplitude. The simulation shows that the value $a(t)k=1$ is reached for $t=2\times10^{-3}$ s. Figures 2(a) and 2(b) give, respectively, the amplitudes and the growth rates of the fundamental, second, and third mode that are obtained from the CADMEE code, the 11th-order approximate theory and the fourth-order full perturbation theory. Figure 2(a) shows that amplitudes obtained from both theories are in good agreement with the numerical simulation. However, it seems that the slopes obtained from the 11th-order approximate theory are better than those given by the fourth-order full perturbation theory. This point is confirmed by looking at Fig. 2(b), where the growth rates are plotted versus time. The agreement between the approximate theory and numerical results is good as long as $t<t_{vs}=1.77\times10^{-3}$ s. On the other hand, the fourth-order full theory deviates from the simulation for $t\approx10^{-3}$ s. In order to quantify the discrepancy between the two theories and the simulation, we have computed the quantity $\Delta_k=\dot{\eta}_{k,\mathrm{theory}}(t)/\dot{\eta}_{k,\mathrm{CADMEE}}(t)-1$, where $\dot{\eta}_k(t)$ is the growth rate of the mode k. Figures 3(a), 3(b), and 3(c) show the discrepancies Δ_k, Δ_{2k}, and Δ_{3k} for the 11th-order approximate perturbation theory and the fourth-order full perturbation theory, versus time. We can see that most of the time, the discrepancies Δ_k and Δ_{2k} remain smaller than 2.5% and 10%, respectively, for the approximate theory. Close to t_{vs}, both discrepancies diverge. Concerning the third harmonics, the discrepancy Δ_{3k} is quite large (but bounded). Let us note that the growth rate of this harmonics is so small that the discrepancy might be meaningless. Figure 3 shows that the fourth-order full perturbation theory is less accurate than the 11th approximate theory.

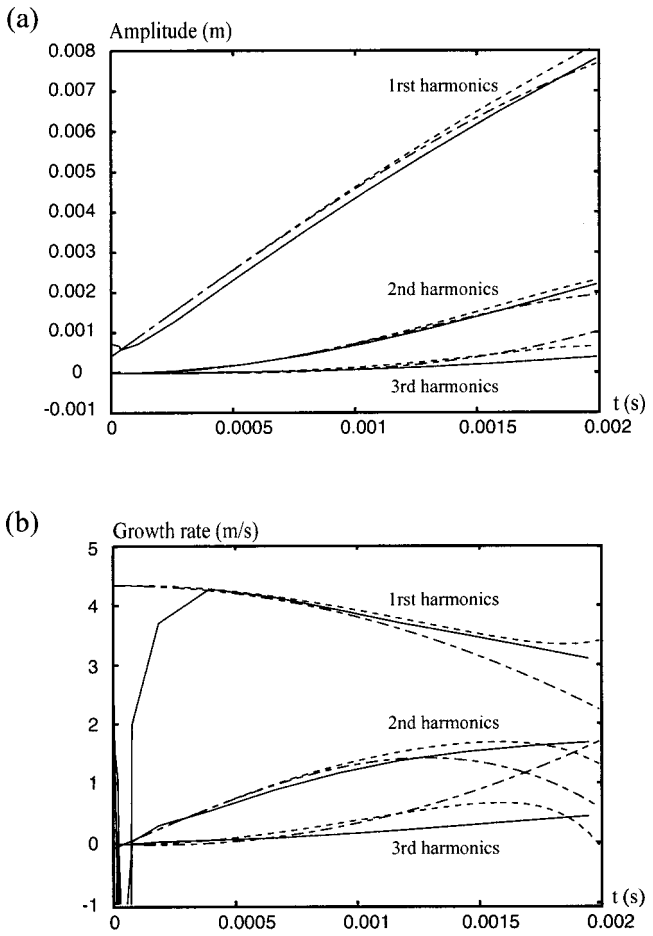

FIG. 2. Spectral analysis of a single-mode perturbation. The (a) amplitude and (b) growth rate of the first three harmonics versus time: full, dashed, and dash–dotted lines represent data from CADMÉE, the 11th-order approximate theory and the fourth-order full theory, respectively. The initial amplitude of the perturbation is positive.

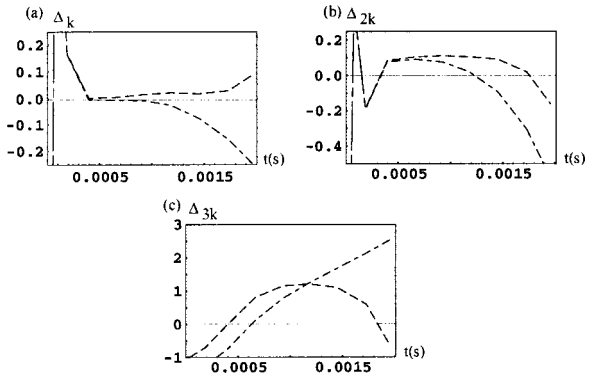

FIG. 3. Discrepancies between the growth rates given by theories and simulation. Dashed and dash–dotted lines represent the 11th-order approximate theory and the fourth-order full perturbation theory, respectively. (a), (b), and (c) stand for the first, second, and third harmonics, respectively.

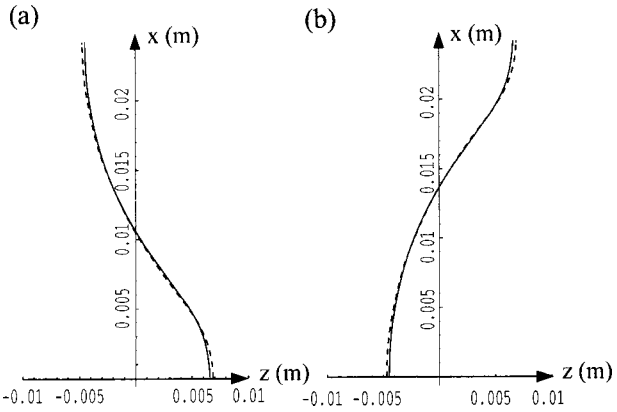

FIG. 5. The shape of the interfaces at $t=1.3\times10^{-3}$ s from theory (dashed line) and simulation (full line). (a) The initial amplitude is positive. (b) The initial amplitude is negative.

In order to prove the influence of the sign of the initial amplitude of the perturbation, a simulation has been performed using the same physical parameter values except for the initial amplitude a_0^-; for the latter, the opposite value is taken: $a_0^- = -0.72\times10^{-3}$ m. Figure 4 gives the growth of the amplitude of the first three modes. Once again, we obtain a good agreement between theory and simulation. It can be seen from comparisons between Figs. 2(a) and 4 that the conclusions that were drawn about the parity of odd and even harmonics with respect to a_0 are verified. This means that the shape of interfaces with positive or negative initial amplitude are not symmetric with respect to the x axis. Indeed, in the linear regime, the shape of an interface stemmed from a negative initial amplitude perturbation can be obtained at any time by using the transform, $a(t)\rightarrow -a(t)$, of the same interface with a positive initial amplitude. In the nonlinear regime, such a symmetry is broken. This is displayed in Fig. 5, where the shape of the interfaces obtained with the theory and the CADMÉE code at $t=1.3\times10^{-3}$ s are shown. Remark that the agreement about the shapes of the perturbations is also good.

The expression of the half peak-to-valley amplitude, $a(t)$, defined by Eq. (9), can be rewritten by using expansions (11). Rearrangement brings the following form for the amplitude $a(t)$:

$$a(t)=a_0+\frac{1}{k}\sum_{\text{odd } i} P_i[A](a_0 k\sigma t)^i, \tag{14}$$

where $P_i[A]$ are polynomials of the ith degree with respect to the Atwood number A. These polynomials are given in Appendix B up to the 11th order. In Fig. 6, the amplitude $a(t)$ is plotted versus time. The full line represents the CADMÉE data. Dashed and dash–dotted lines represent theoretical results at the ninth and 11th order, respectively. The agreement between simulation and theory is good as long as time remains smaller than t_{vs} (see the vertical line in Fig. 6). After that time, the perturbation series diverges. It has been checked in this example that terms that are not taken into account in the theoretical approach are indeed negligible. On this configuration, the approximate perturbation method is accurate, as it has been shown by comparing with 2-D numerical simulations. In addition to the evolution of the peak-to-valley amplitude, the approximate perturbation theory also gives access to the expressions for the spike and bubble

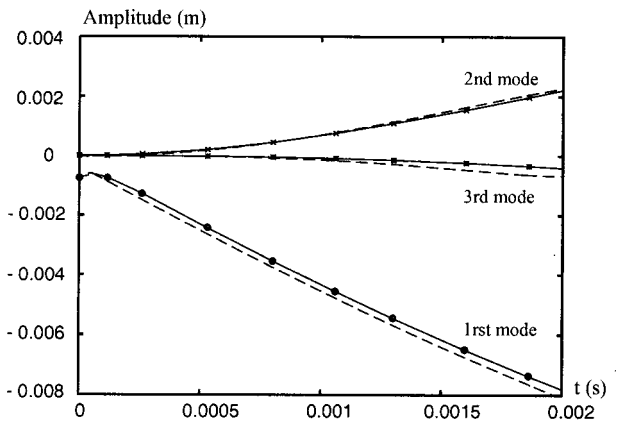

FIG. 4. The same as in Fig. 2(a), but the initial amplitude of the perturbation is negative.

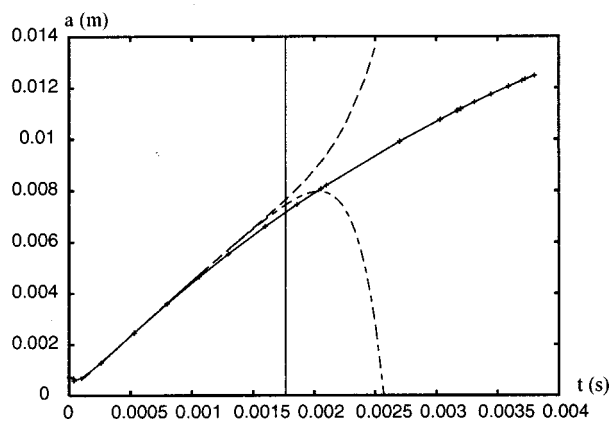

FIG. 6. The half-peak-to-valley amplitude versus time in the single-mode configuration. A full line represents numerical simulation data. Dashed line and dash–dotted lines represent theoretical results at the ninth and 11th order, respectively.

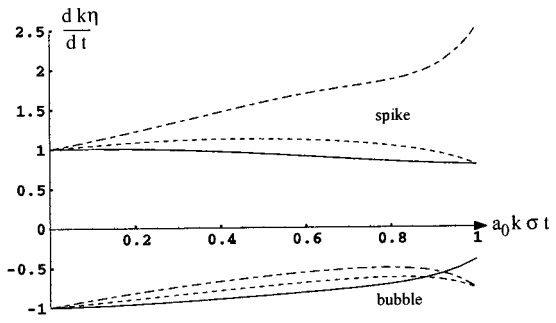

FIG. 7. Nondimensionalized growth rates for the spike and the bubble against the scaled time $a_0 k\sigma t$. Results are from the 11th-order approximate theory. Full, dotted, and dash–dotted lines are plotted for three different Atwood numbers: $A=0.1$, 0.48, and 1.

growths. In Fig. 7, we have plotted the nondimensionalized growth rates $k\dot{\eta}_{\text{spike}}$ and $k\dot{\eta}_{\text{bubble}}$ against the quantity $a_0 k\sigma t$, for three different Atwood numbers: $A=0.1$, 0.48, and 1. Several conclusions can be drawn from Fig. 7. First, the growth rate of the bubble is slightly dependent on the Atwood number. Second, for a small Atwood number, the growths of spike and bubble have approximatively the same absolute value; this should lead to a symmetric pattern. Third, for large values of the Atwood number, the spike has a higher growth rate than the one of the bubble. These conclusions about the influence of the Atwood number upon the relative growth rates of spike and bubble are in qualitative good agreement with the nonlinear RM experiments described in Ref. 23. In these experiments, the growth rates of two configurations with Atwood numbers $A=0.48$ and 0.92 are presented. First, the growths of bubbles for both configurations seem to be the same. Second, for the $A=0.48$ configuration, the growths of spike and bubble are similar. Third, for the $A=0.92$ configuration, the spike grows faster than the bubble. So, even if these experiments are in the intermediate nonlinear regime where the approximate perturbation theory is no more valid, it seems that this theory brings qualitatively reliable information about the relative growths of spike and bubble. Such a qualitative agreement beyond the weakly nonlinear regime will also be presented in Sec. IV B. The variation of the spike growth rate versus the Atwood number is not found by Volkov *et al.*[24]

III. PERTURBATION EXPANSIONS FOR MULTIMODE CONFIGURATIONS

A. Derivation of the approximate perturbation theory

We now study an interface that is initially composed of N modes of wave number k_i with respective initial post-shocked amplitude a_{0i}. The shape of this interface is written as

$$\eta(x,0)=\sum_{i=1}^{N} a_{0i}\cos k_i x.$$

According to the sign of the amplitudes, the modes have the same or opposite phase. The linear growth rate of such an interface is given by

$$\eta^{(1)}(x,t)=\sum_{i=1}^{N} a_{0i}\sigma_i t\cos k_i x.$$

In order to obtain expressions with the same form as Eqs. (11), a specific mode k_1 is selected and factorized. As σ_i is proportional to the wave number k_i, the first-order expansion of $\eta(x,t)$ can be written as

$$k_1\eta^{(1)}(x,t)=(a_{01}k_1\sigma_1 t)\sum_{i=1}^{N} a_i^{(1)}\cos k_i x,$$

with $a_i^{(1)}=(a_{0i}/a_{01})(k_i/k_1)$. By analogy with Eqs. (11), we assume the following form for the nth order of $\eta(x,t)$:

$$k_1\eta^{(n)}(x,t)=(a_{01}k_1\sigma_1 t)^n\sum_{i=1}^{l_n} a_i^{(n)}\cos k_i^{(n)}x, \tag{15}$$

where $k_i^{(n)}$ are the wave numbers present at the nth order and l_n is the mode count at the same order. These modes are obtained from two-by-two addition and subtraction of the modes present at the $(n-1)$th order. The same kind of factorization and analogy is used in order to obtain expressions of $\Phi^{(n)}$ and $\Phi'^{(n)}$ for the multimode case.

The algorithm to solve Eqs. (3), (4), and (5) for the multimode case is the same as for the single-mode case. Subscripts of summations now vary from 1 to l_n instead of 1 to n. We now summarize this algorithm.

(i) Expansions such as Eq. (15) are used in Eqs. (3)–(5) for $\eta^{(n)}$, $\Phi^{(n)}$, and $\Phi'^{(n)}$.

(ii) At the nth order, only terms with t^{n-1} dependence for Eqs. (3) and (4), and t^{n-2} dependence for Eq. (5) are retained. This comes from the properties of the most secular terms.

(iii) The resulting system is projected on the cosine base $\{\cos k_i^{(n)}x, 0\leqslant i\leqslant l_n\}$. The l_n+1 resulting systems are algebraic and linear. They are easily solved and the $3(l_n+1)$ real unknowns $(a_i^{(n)}, b_i^{(n)}, b_i'^{(n)})$ are obtained.

From a technical point of view, the generalization from the single-mode algorithm to the multimode one only requires to change the subscripts of the series and to compute the modes that appear at each order. This is easily handled by symbolic computation softwares. We emphasize that the approximate theory does not require time integration and strongly reduces storage space. This means that the evolution of a multimode interface can now be handled. The range of validity, t_{vm}, of this N-mode configuration is assumed to be the smallest t_{vs} of the N configurations, where the modes are taken independently. So t_{vm} is written as $t_{vm}=\text{Min}\{(a_{0i}k_i\sigma_i)^{-1}, 1\leqslant i\leqslant N\})$. We did check this assumption numerically.

B. Numerical applications: Quantitative results

We now study a three-mode interface. In order to increase the coupling between modes, we choose k_1, k_2, and k_3 such that $k_2+k_3=k_1$. In this example, $k_1=274.855\,\text{m}^{-1}$, $k_2=3/7k_1$, and $k_3=4/7k_1$. By doing so, at the second order, the mode k_1 is generated by the harmonics k_2+k_3. This generation may lead to a stronger influence

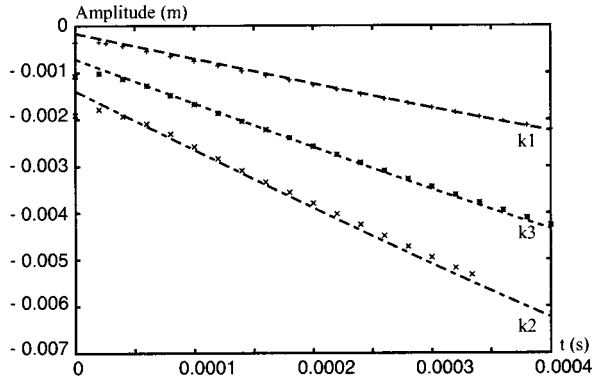

FIG. 8. Single-mode dynamics. The half-peak-to-valley amplitude of the three modes versus time. The initial amplitudes are negative. Symbols represent numerical data. Dashed lines represent seventh-order theoretical results. The range of validity of the theory is $t_{vm}=0.67\times10^{-3}$ s.

on the mode k_1. The initial post-shocked amplitudes are $a_{01}=-0.35\times10^{-3}$ m, $a_{02}=-1.9055\times10^{-3}$ m, and $a_{03}=-1.072\times10^{-3}$ m. In this configuration, a 1.0962 Mach number shock wave moves from helium to air. The initial pressure is 1.013×10^{5} Pa. The pre-shocked and post-shocked Atwood numbers are 0.757 and 0.764, respectively. With this choice of physical parameter values, $t_{vm}=0.67\times10^{-3}$ s. In the following, theoretical results are produced by seventh-order perturbation expansions.

Figure 8 shows the growth of the amplitude of each mode in a single-mode configuration, i.e., obtained from separate numerical simulations. Symbols correspond to the CADMÉE calculations and dashed lines to the approximate theory. It can be checked that the theory is accurate as long as t remains smaller than t_{vm}. Figure 9 presents the evolution versus time of each mode when they are initially put together. The agreement between theory and 2-D simulations is good. The growth of the mode k_1 is strongly reduced when it interacts with the two other modes. As previously underlined, this behavior is due to the fact that the wave numbers satisfy $k_2+k_3=k_1$. Indeed, the growth of this sum mode counteracts the evolution of the initial mode k_1. On the other hand, the two other modes seem to grow according to their single-mode dynamics.

We now emphasize the role of the phase of the modes. To this end, a new three-mode simulation has been run with

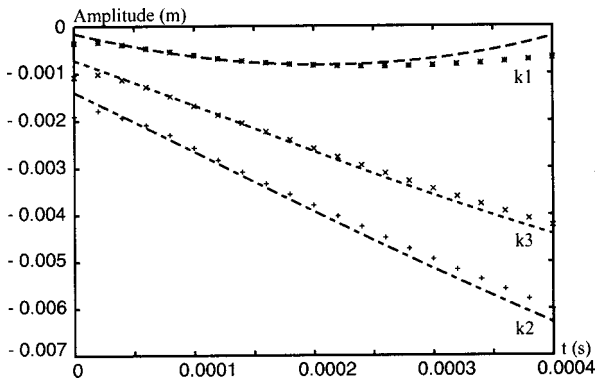

FIG. 9. The same as in Fig. 8 but the three modes interact.

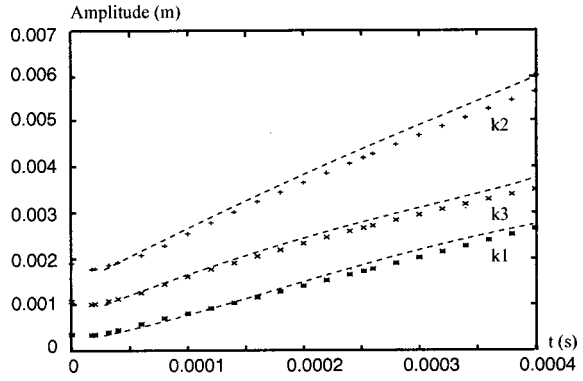

FIG. 10. The same as in Fig. 9, but the modes have positive initial amplitudes.

the same parameter values as in the previous case, except for the sign of the amplitudes. We now have $a_{01}=+0.35\times10^{-3}$ m, $a_{02}=+1.9055\times10^{-3}$ m, and $a_{03}=+1.072\times10^{-3}$ m. Figure 10 presents the evolution versus time of the amplitude of the three interacting modes. By comparing Fig. 9 with Fig. 10, different coupling effects can be seen: the growth of the mode k_3 is now slightly reduced while the mode k_1 seems to be unaffected. The behavior of the mode k_1 is strongly linked to the value of the phase. As seen in Sec. II D, the phase determines the sign of the amplitude of the harmonics; depending of their sign, the harmonics will reduce or not the growth of existing modes. This example illustrates the fact that the mode selection process is not only determined by the values of the modes and their amplitudes, but also by the phase of these modes.

IV. INFERENCES FOR THE INTERMEDIATE NONLINEAR STAGE

A. Padé approximants and perturbation theories

As shown in Sec. II, the secular terms in perturbation series make these series to diverge at some finite time. One example of this divergence is presented in Fig. 6. In order to improve the convergence of such series, summation methods are commonly used. Since only a few terms are available, one has to resort to appropriate algorithms; one of them is the well-known Padé approximant.[17] For the growth rate of the amplitude of a single-mode interface, Padé approximants, P_1^0 and P_2^0, can be calculated from the second- and the fourth-order expansions, respectively. Zhang and Sohn combine P_1^0 and P_2^0 obtained from the full perturbation theory in order to obtain the following practical expression:[12,13]

$$\frac{da}{dt}=\frac{a_0\sigma}{1+(a_0k)^2\sigma t+\mathrm{Max}\{0,a_0^2k^2-A^2+1/2\}(a_0k\sigma t)^2}. \tag{16}$$

Equation (16) corresponds to Eq. (53) of Ref. 12 or Eq. (87) of Ref. 13. Reasons for such a combination are detailed in Refs. 12 and 13. Indeed, a time singularity may occur in P_2^0. So, parameter regions defined by $a_0^2k^2<A^2-\frac{1}{2}$ and $a_0^2k^2\geqslant A^2-\frac{1}{2}$ are differentiated. The Zhang and Sohn point of view is that "*there are two conventional ways to remove a singularity. One is to reduce the order of accuracy by taking*

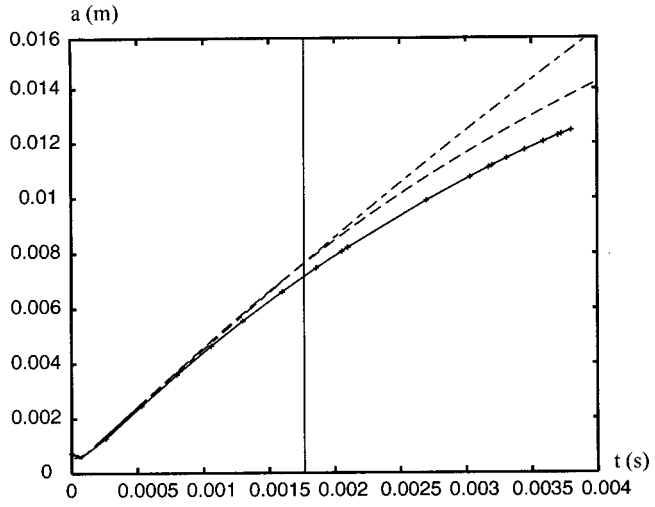

FIG. 11. The half-peak-to-valley amplitude versus time in the single-mode configuration. The full line represents numerical data. Dash–dotted and dashed lines are plotted from Eq. (14) and the P_6^4 Padé approximant, respectively.

less terms and the other one is to take more terms.''[13] As a result, they choose P_1^0 instead of P_2^0 in order to remove the singularity. It is better, as far as it is possible, to use higher-order Padé approximants. For example, 11th-order approximate perturbation theory allows us to build the P_6^4 Padé approximant. One example of such an application is now presented.

In numerous cases, Eq. (16) is enough to predict the nonlinear growth rate even if the order of the Padé approximant is low. However, some cases can be found where a fourth-order Padé approximant is not accurate enough. In order to illustrate that point, we use the same physical parameter values[22] as the ones used to obtain the results displayed in Fig. 6. As mentioned above, a P_6^4 Padé approximant is used in order to improve the convergence of $\dot{a}(t)$ obtained from Eq. (14). The growth rate is then time integrated in order to get the growth of the amplitude. In Fig. 11, we have plotted the results that are obtained from CADMÉE. They have to be compared with time integrations of Eq. (16) from the standard theory and the P_6^4 Padé approximant from the approximate theory. First, as expected, curves obtained with Padé approximants do not diverge beyond $t_{vs}=1.77\times10^{-3}$ s (see Fig. 6 for a comparison). However, the growth given by Eq. (16) shows no significant decaying and therefore does not agree with the simulation. On the other hand, the growth given by the P_6^4 Padé approximant exhibits a saturation behavior and is in quite good agreement with the 2-D simulation. This decaying growth rate is a common feature of nonlinear RM dynamics. Only the high-order Padé approximant seems to be able to produce such a feature. So, even if a P_2^0 or a P_1^0 approximant can give good approximations of the growth for numerous cases,[12,25] for other ones, higher-order Padé approximants are required in order to produce reliable predictions.

B. Selection mode process: Qualitative results

We have seen that the perturbation theory derived in previous sections has a finite range of validity. This range of validity can be increased with summation algorithms such as Padé approximants. Let us remark that such methods provide only approximate results and that discrepancies from 2-D simulations can become very large at large time (see, for example, Fig. 11). Moreover, at such times, mushroom-like structures may appear whereas the theory can only describe single-mode interfaces.

On the other hand, an important issue in nonlinear interaction studies is to understand the mode selection process, i.e., which modes become dominant or are suppressed during the interaction. In this section, we will see that using the approximate theory beyond the weakly nonlinear regime allows us to obtain qualitative results about the selection mode process. As shown in Sec. III B, Fourier modes already interact in the early nonlinear stage. In order to study the late time interaction of two modes, we follow the same methodology that the one used in Ref. 26 about the Rayleigh–Taylor instability. In this paper, 2-D numerical simulations provide the time evolution of the shape of the interfaces that are then Fourier analyzed. Two cases are discussed: a nearby mode configuration ($k_2/k_1=\frac{8}{7}$) and a dissimilar mode configuration ($k_2/k_1=\frac{7}{2}$). The growth of the competing modes is compared with their single-mode dynamics.

For the RM instability, the range of validity of the approximate theory, checked numerically, scales as k^{-2}. For the dissimilar mode configuration, this greatly complicates the study at late time since the ranges of validity for the single-mode and the two-mode configurations may be quite different. On the other hand, this constraint does not arise for the nearby mode case and its study with the approximate theory is straightforward. Therefore and for practicality, we only present in this paper a nearby mode study. In a first step, 2-D simulations of RM instability are performed with the code CADMÉE. In these configurations, a 1.26 Mach number shock wave moves from helium to air. The two wave numbers of the initial interface perturbation are $k_1=274.889\,\mathrm{m}^{-1}$ and $k_2=314.159\,\mathrm{m}^{-1}$. The initial amplitude for each mode is either $a_{01}^-=10^{-3}$ m or $a_{02}^-=0.35\times10^{-3}$ m. The post-shocked Atwood number is $A=0.756$. The ranges of validity for the following single-mode (k,a_0^-) configurations: (k_1,a_{01}^-), (k_1,a_{02}^-), (k_2,a_{01}^-), (k_2,a_{02}^-), are 8.5×10^{-5}, 2.43×10^{-4}, 6.5×10^{-5}, and 1.85×10^{-4} s, respectively. The final time of the 2-D simulations is 1.8×10^{-3} s. At time as early as $t=4.\times10^{-4}$ s, mushroom-like features appear at the interface. This can be seen in Fig. 12, which shows the isocurves $c=0.25$, $c=0.5$, and $c=0.75$ at different times for the following two-mode configuration: $\{(k_1,a_{01}^-),(k_2,a_{02}^-)\}$. In order to perform the spectral analysis of such shapes, we use the same method as in Ref. 26. The z-integrated density distribution is computed, $\rho(x)=\int\rho(z,x)dz$. The Fourier transform of this distribution is then taken. This procedure is accurate at early time. At late time, when mushrooming appears, the z integration suppresses small structures and the growth of small wavelengths is roughly estimated; but we believe that this analysis re-

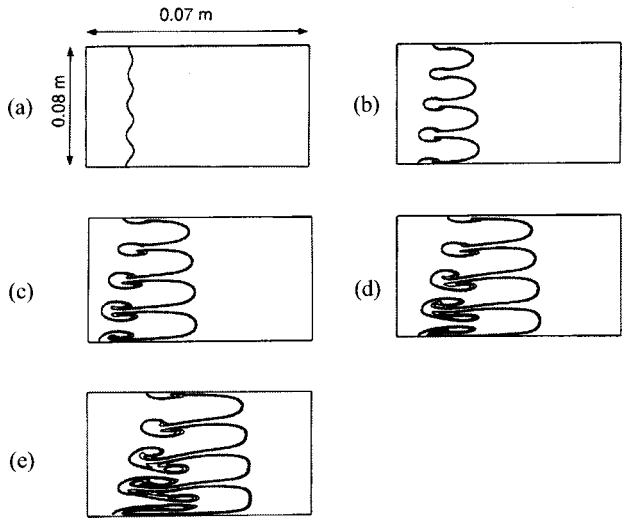

FIG. 12. One of the two-mode configurations: $(k_1, a_{02}^-) = (274.889\ \mathrm{m}^{-1}, 0.35\times10^{-3}\ \mathrm{m})$ and $(k_2, a_{01}^-) = (314.159\ \mathrm{m}^{-1}, 10^{-3}\ \mathrm{m})$. The two gases are helium and air. Interface shapes for $t=0$ (a), 0.4 ms (b), 0.8 ms (c), 1.2 ms (d) and 1.6 ms (e).

mains valid for the computations of the main components of the spectrum. Figures 13(a), 13(c), 13(e), and 13(g) show the results obtained from numerical simulations and compare the single-mode evolution with the two-mode growth of k_1 and k_2 for various initial amplitudes. Full and dashed lines represent single- and two-mode dynamics, respectively. From the simulation results, the values of the initial amplitudes seem to dictate the selection process: the mode with the lower initial amplitude is suppressed. When the initial amplitudes are the same, the growths of modes k_1 and k_2 are similarly reduced by the interaction. These conclusions are the same as the ones obtained in Ref. 26 about the Rayleigh–Taylor instability. Figures 13(b), 13(d), 13(f), and 13(h) show the growths of k_1 and k_2 that are obtained with the P_2^1 Padé approximant of the fifth-order approximate perturbation expansion. Vertical bars on each curve indicate the range of validity of the perturbation expansion. It can be verified that theoretical and numerical results are in good agreement in the range of validity of the theory. Beyond that time, the P_2^1 Padé approximant exhibits an oversaturated behavior: at large time, the growth from the extended approximate theory is roughly half the simulation values. However, the following qualitative remarks can be drawn.

(i) Figures 13(a) and 13(b) deal with the configuration $(k_1, a_{02}^-) = (274.889\ \mathrm{m}^{-1}, 0.35\times10^{-3}\ \mathrm{m})$ and $(k_2, a_{01}^-) = (314.159\ \mathrm{m}^{-1}, 10^{-3}\ \mathrm{m})$. For the single-mode dynamics, the relative evolution of the two modes is qualitatively recovered by the theory. In the simulation of the two-mode dynamics, the mode k_1 is suppressed, whereas the mode k_2 behavior is only slightly modified by the interaction. In the same way, theoretical results show that the growth of the mode k_1 saturates whereas the mode k_2 is not perturbed.

(ii) Figures 13(c) and 13(d) deal with the configuration (k_1, a_{01}^-), (k_2, a_{02}^-). The relative evolution of the modes in

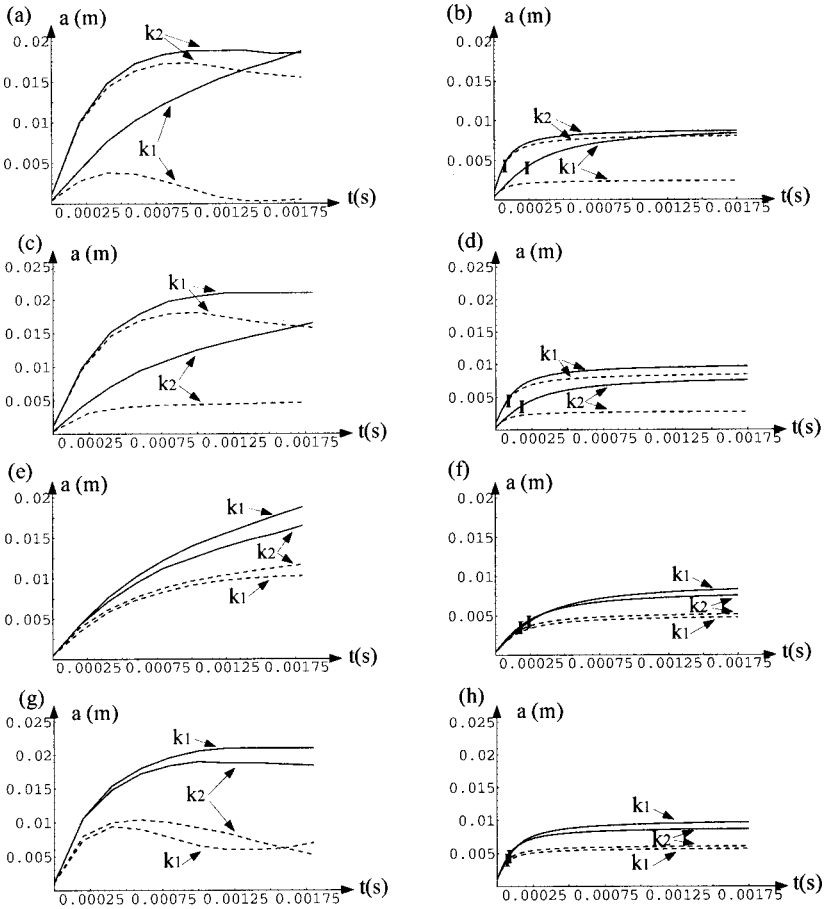

FIG. 13. Single- and two-mode configurations. Growth of the modes k_1 and k_2 versus time. Full and dashed lines represent the single-mode and two-mode dynamics, respectively. Curves (a), (c), (e), and (g) are obtained from CADMÉE simulations. Curves (b), (d), (f), and (h) are from the approximate perturbation theory.

their single-mode dynamics is similar in both theoretical and simulation results. When the two-mode dynamics is considered, the mode k_2 saturates, whereas the mode k_1 is only slightly perturbed. These behaviors are also found theoretically.

(iii) Figures 13(e) and 13(f) deal with the configuration (k_1, a_{02}^-), (k_2, a_{02}^-). In this configuration, there is no dominant mode. However, the growth of the two modes is lowered by the interaction. Note that the mode k_1 has a higher amplitude than the one of the mode k_2 at large time in the single-mode dynamics and a lower one in the two-mode dynamics. These behaviors are recovered with the theory, despite the underestimated growths.

(iv) Figures 13(g) and 13(h) deal with the configuration (k_1, a_{01}^-), (k_2, a_{01}^-). The same conclusions as in the previous item can be drawn for this configuration.

We believe that the good qualitative agreement about the mode behavior indicates that mechanisms of the selection process are already present at an early time, i.e., the mode selection process is driven by early time dynamics. Therefore, this nearby mode study shows that the approximate perturbation theory can be a useful tool to understand the origins of the late time selection of modes.

C. Class of homothetic interfaces

In this section, we describe some properties established from the weakly nonlinear theory. The 2-D numerical simulations show that these properties are still valid in the intermediate nonlinear stage. To this end, the expression (14) of the amplitude of a single-mode interface is rearranged as follows:

$$k[a(t)-a_0]=\sum_{i=1}^{\infty} P_i[A](a_0 k\sigma t)^i,$$

$$\text{with } P_i=0, \quad \text{for even } i. \tag{17}$$

The right-hand side of Eq. (17) can be considered as the Taylor expansion of a single function $\mathcal{F}$ that depends on two variables, A and $a_0 k\sigma t$,

$$\begin{aligned}\mathcal{F}(A,a_0 k\sigma t)&=\sum_{i=1}^{\infty} \frac{1}{i!}\frac{\partial^i \mathcal{F}}{\partial(a_0 k\sigma t)^i}\bigg|_0 (a_0 k\sigma t)^i\\ &=\sum_{i=1}^{\infty} P_i[A](a_0 k\sigma t)^i\\ &=k[a(t)-a_0].\end{aligned} \tag{18}$$

Equation (18) means that if two interfaces have the same Atwood number, A, and the same value of the product $a_0 k\sigma$, their time history will be linked by $\mathcal{F}$. An easy way to obtain such conditions is to deal with the same base flow. This leads to the same Atwood number. In order to obtain the same value of $a_0 k\sigma$, as σ is proportional to k, it is sufficient to use the same value of $a_0 k^2$. So, when the same physical parameter values are used, Eq. (18) can be applied to two configurations 1 and 2, and gives

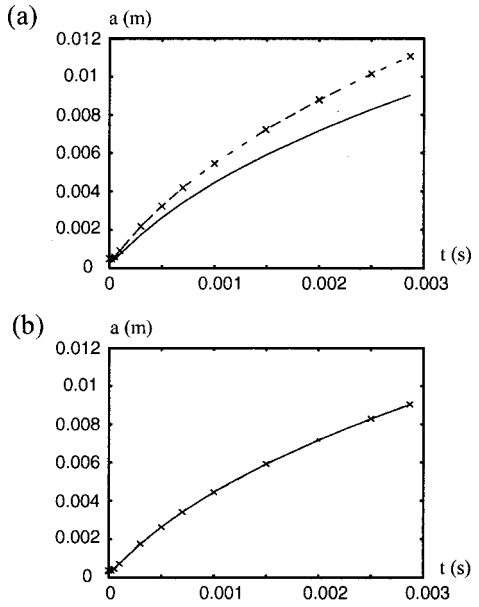

FIG. 14. Homothetic single-mode dynamics. (a) Growths of the perturbations 1 and 2 are plotted with full and mark-dotted lines, respectively. Results are obtained with the CADMÉE code. (b) The growth of the perturbation 1. The full line is from the CADMÉE simulation. The mark-dotted curve is obtained from perturbation 2 by using Eq. (19).

$$a_2(t)=\frac{k_1}{k_2}(a_1(t)-a_{01})+a_{02} \quad \text{if } a_{01}k_1^2=a_{02}k_2^2. \tag{19}$$

Equation (19) defines a class of homothetic configurations: for a given set of physical parameters, the growth of one configuration allows us to determine the growth of all the configurations of the same class.

In order to confirm this conclusion, we have run two simulations with the CADMÉE code.

The physical parameters are the same as those used in Sec. III B. The two configurations are the following: $(a_{01},k_1)=(0.35\text{ mm},274.855)$ and $(a_{02},k_2)=(0.525\text{ mm}, 224.418)$, which satisfies the equality $a_{01}k_1^2=a_{02}k_2^2$. The simulations utilize the same number of nodes: the mesh size for the configuration 2 is, respectively, 1.5 and 1.225 times as large as the one for configuration 1 in the z and x directions, respectively. Figure 14(a) shows the growths of the perturbations obtained from the 2-D simulations. Full and mark-dotted lines represent configurations 1 and 2, respectively. Figure 14(b) shows the growths of the perturbation 1 obtained either from the simulation (full line) or from Eq. (19). Agreement between the simulation and the transformed curve is excellent: the two results cannot be distinguished. The range of validity of the approximate theory for these two configurations is $t_{vs}=0.72\times10^{-3}$ s. Figure 14(b) shows that Eq. (19), which is drawn from a weakly nonlinear theory, is still valid in the intermediate nonlinear regime. Furthermore, even when mushroom shapes appear, the homothetic transform allows us to determine one interface shape from the other one. Figure 15(a) shows the shapes of the interfaces 1 and 2 at $t=2.87\times10^{-3}$ s (full and mark-dotted lines, respectively). We have applied z and x homotheties of scale $k_2/k_1=0.82$ to the shape 2. The result is plotted in a mark-

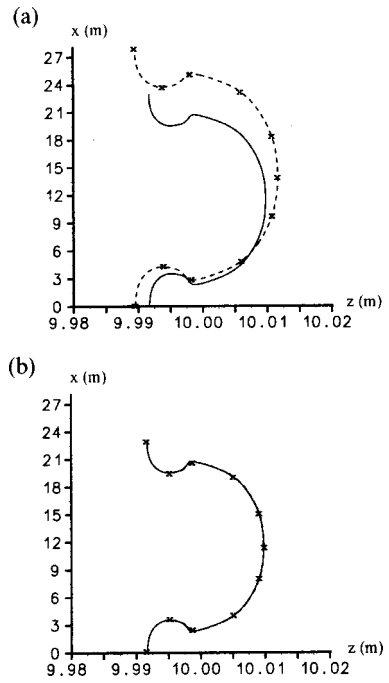

FIG. 15. Homothetic single-mode dynamics at $t=2.87\times10^{-3}$ s. (a) Shapes of perturbations 1 and 2 are plotted with full and mark-dotted lines, respectively. Results are obtained with the CADMEE code. (b) Shape of the perturbation 1. The full line is from CADMEE simulation. The mark-dotted curve is obtained from a homothetic transform of shape 2.

dotted line in Fig. 15(b). It has to be compared with the shape 1 in a full line. Once again, the agreement is excellent, even for the vortex structures of the mushroom. As shown in the previous example, the class of homothetic perturbations that was established in the weakly nonlinear regime still stand in a later time nonlinear regime. Previous conclusions bring useful simplifications. First, from a numerical point of view, a larger mesh size implies less limiting CFL conditions.[27] The time step is larger and the simulation requires less CPU time. This has been verified with the simulations for the two previous configurations 1 and 2: the latter used 22% less CPU time than the former. This is consistent with the scaling carried out on the mesh size. Second, from an experimental point of view, RM experiments have been conducted on laser facilities for ICF applications.[25,28,29] The classical perturbation theory have already been used in order to understand some of these experimental results.[25] Homothetic configurations could palliate the limitation of spatial resolution of ICF diagnostics. Their typical resolution is 10 μm. Thus, a perturbation with a wavelength $\lambda_\alpha=10\,\mu$m and an amplitude $a_{0\alpha}=0.1\,\mu$m could not be studied with an x-ray imager. On the other hand, the homothetic perturbation $\lambda_\beta=31.62\,\mu$m and $a_{0\beta}=1\,\mu$m could easily be studied. With the use of Eq. (19), it could give the growth of the former perturbation. With the same reasoning, and if the same Atwood number and the same value of the product $a_0k\sigma$ are obtained, ICF-size RM instabilities could be studied with gas shock tubes: the two previous ICF-size perturbations could be replaced with the following perturbation: $\lambda_\gamma=1$ cm and $a_{0\gamma}=4$ mm. Standard shock tube facilities can easily deal with such perturbations.

V. CONCLUDING REMARKS

We have developed an efficient way of deriving a perturbation method for the Richtmyer–Meshkov instability in the nonlinear regime. This model holds provided the flows are potential and incompressible. Solutions have been obtained as perturbation expansions with respect to the small parameter a_0k, i.e., the wave steepness. As time derivatives are involved in the equations and since the linear growth rate is constant, previous perturbation expansions appear to be series in integer powers of time. Such expansions can be drastically simplified by retaining, at each order, the terms with the highest power in time. Nonlinear behavior of single-mode interfaces can then be easily calculated, even if high-order expansions are required. In a similar way, the calculation of the nonlinear regime of a multimode RM instability becomes tractable. Several conclusions can be drawn from this study.

(i) The range of validity of the theory, checked numerically, is t_{vs} with $a_0k\sigma t_{vs}=1$ for the single-mode case. The convergence of series can be improved by summation techniques such as Padé approximants.

(ii) It is worth noticing that $a(t_{vs})k\approx1$. Note that the limit $a(t)k=1$ was previously and empirically used as the end of the linear regime.

(iii) The nonlinear behavior of an interface strongly depends on the sign of the amplitude of the modes. We have shown that, all other things being equal, changing the sign of the amplitudes leads to different dominant modes. Furthermore, strong interactions can occur since the weakly nonlinear regime.

(iv) It turns out that the selection process in the nonlinear regime can be predicted from the weakly nonlinear theory. Padé approximants, despite an oversaturated growth for the mushroom-like stage, allow us to predict the wave number of the leading mode. This has been verified with comparisons between theory and simulation for a two-mode interface.

(v) Within such theory, we are able to define homothetic interfaces. For single-mode configuration, homothetic interfaces have the same values of a_0k^2 and A. For two perturbations of the same class, the ratio of the time-dependent amplitudes is the ratio of the wavelengths. Moreover, 2-D simulations in the intermediate nonlinear regime have shown that the shapes of single-mode interfaces scale as the ratio of the wavelengths.

The kind of solution technique that has been used in this paper is appropriate to describe instabilities that steadily grow versus time. On the other hand, others methods should be used in order to deal with chaotic solutions such as the ones occurring, for example, in subcritical transitions.

This approximate perturbation method can be extended to three-dimensional configurations. It can also be applied to Rayleigh–Taylor-like instabilities such as, for example, multi-interface configurations or ablation front instability.

APPENDIX A: LIST OF COEFFICIENTS $a_j^{(i)} \equiv a[j,i]$ UP TO THE SEVENTH ORDER FOR A SINGLE-MODE PERTURBATION

All the values that are not specified below are null.

$$a[1,1]=1;$$

$$a[2,2]=A/2;$$

$$a[1,3]=(-1-4*A\hat{}2)/24;$$

$$a[3,3]=(-1+4*A\hat{}2)/8;$$

$$a[2,4]=-A\hat{}3/3;$$

$$a[4,4]=(A*(-1+2*A\hat{}2))/3;$$

$$a[1,5]=(1+60*A\hat{}2+16*A\hat{}4)/960;$$

$$a[3,5]=(3*(5+40*A\hat{}2-144*A\hat{}4))/640;$$

$$a[5,5]=(21-296*A\hat{}2+400*A\hat{}4)/384;$$

$$a[2,6]=(A*(-17+90*A\hat{}2+72*A\hat{}4))/720;$$

$$a[4,6]=(11*A+277*A\hat{}3-512*A\hat{}5)/360;$$

$$a[6,6]=(A*(23-140*A\hat{}2+144*A\hat{}4))/80;$$

$$a[1,7]=(-337-7612*A\hat{}2+3712*A\hat{}4+1536*A\hat{}6)/322560;$$

$$a[3,7]=(107-16100*A\hat{}2+15680*A\hat{}4+43264*A\hat{}6)/107520;$$

$$a[5,7]=(-1129-10220*A\hat{}2+158224*A\hat{}4-200000*A\hat{}6)/64512;$$

$$a[7,7]=(-1605+48988*A\hat{}2-184240*A\hat{}4+153664*A\hat{}6)/46080.$$

APPENDIX B: LIST OF POLYNOMIALS $P_i[A]$ INVOLVED IN THE EXPRESSION OF THE AMPLITUDE OF A SINGLE-MODE INTERFACE

$$P1[A]=1;$$

$$P3[A]=(-1+2*A\hat{}2)/6;$$

$$P5[A]=(19-125*A\hat{}2+92*A\hat{}4)/240;$$

$$P7[A]=(-264+3686*A\hat{}2-6997*A\hat{}4+3234*A\hat{}6)/5040;$$

$$P9[A]=(117663-2855274*A\hat{}2+10086083*A\hat{}4-11093856*A\hat{}6+3805728*A\hat{}8)/2903040;$$

$$P11[A]=(-5507319+206796915*A\hat{}2-1168865775*A\hat{}4+2250383605*A\hat{}6-1755444326*A\hat{}8+483163144*A\hat{}10)/159667200.$$

[1] R. D. Richtmyer, "Taylor instability in shock acceleration of compressible fluids," Commun. Pure Appl. Math. **13**, 297 (1960).
[2] E. E. Meshkov, "Interface of two gases accelerated by a shock wave," Fluid Dyn. **4**, 101 (1969).
[3] G. Fraley, "Rayleigh–Taylor stability for a normal shock wave-density discontinuity interaction," Phys. Fluids **29**, 376 (1986).
[4] K. O. Mikaelian, "Freeze-out and the effect of compressibility in the Richtmyer–Meshkov instability," Phys. Fluids **6**, 356 (1994).
[5] Y. Yang, Q. Zhang, and D. H. Sharp, "Small amplitude theory of Richtmyer–Meshkov instability," Phys. Fluids **6**, 1856 (1994).
[6] A. L. Velikovich, "Analytic theory of Richtmyer–Meshkov instability for the case of reflected rarefaction wave," Phys. Fluids **8**, 1666 (1996).
[7] J. G. Wouchuk and K. Nishihara, "Linear perturbation growth at a shocked interface," Phys. Plasmas **3**, 3761 (1996).
[8] J. G. Wouchuk, "Growth rate of the linear Richtmyer–Meshkov instability when a shock is reflected," Phys. Rev. E **63**, 056303 (2001).
[9] A. H. Nayfeh, *Perturbation Methods* (Wiley, New York, 1973).
[10] R. L. Ingraham, "Taylor instability of the interface between superposed fluids—Solution by successive approximations," Proc. R. Soc. London, Ser. B **67**, 748 (1954).
[11] S. W. Haan, "Weakly nonlinear hydrodynamic instabilities in inertial fusion," Phys. Fluids B **3**, 2349 (1991).
[12] Q. Zhang and S-I. Sohn, "Nonlinear theory of unstable fluid mixing driven by shock wave," Phys. Fluids **9**, 1106 (1997).
[13] Q. Zhang and S.-I. Sohn, "Quantitative theory of Richtmyer–Meshkov instability in three dimensions," Z. Angew. Math. Phys. **50**, 1 (1999).
[14] A. L. Velikovich and G. Dimonte, "Nonlinear perturbation theory of the incompressible Richtmyer–Meshkov instability," Phys. Rev. Lett. **76**, 3112 (1996).
[15] U. Alon, J. Hecht, D. Ofer, and D. Shvarts, "Power laws and similarity of Rayleigh–Taylor and Richtmyer–Meshkov mixing fronts at all density ratios," Phys. Rev. Lett. **74**, 534 (1995).
[16] J. D. Ramshaw, "Simple model for linear and nonlinear mixing at unstable fluid interfaces with variable acceleration," Phys. Rev. E **58**, 5834 (1998).
[17] C. M. Bender and S. A. Orszag, *Advanced Mathematical Methods for Scientists and Engineers* (McGraw-Hill, New York, 1978).
[18] K. A. Meyer and P. J. Blewett, "Numerical investigation of the stability of a shock-accelerated interface between two fluids," Phys. Fluids **15**, 753 (1972).
[19] M. Vandenboomgaerde, C. Mügler, and S. Gauthier, "Impulsive model for the Richtmyer–Meshkov instability," Phys. Rev. E **58**, 1874 (1998).
[20] J. Kevorkian and J. D. Cole, *Perturbation Methods in Applied Mathematics* (Springer-Verlag, New York, 1981).
[21] C. Mügler, L. Hallo, S. Gauthier, and S. Aubert, "Validation of an ALE Godunov algorithm for solutions of the two-species Navier–Stokes equations," AIAA Paper 96-2068, 1996.
[22] R. F. Benjamin, "Experimental observations of shock stability and shock-induced turbulence," in *Advances in Compressible Turbulent Mixing*, Proceedings of the 1st International Workshop on the Physics of Compressible Turbulent Mixing, edited by W. P. Dannevik, A. C. Buckingham, and C. E. Leith (Lawrence Livermore National Laboratory, Livermore, CA, 1992), Conf-8810234, pp. 341–348.
[23] G. Dimonte, "Nonlinear evolution of the Rayleigh–Taylor and Richtmyer–Meshkov instabilities," Phys. Plasmas **6**, 2009 (1999).
[24] N. B. Volkov, A. E. Maier, and A. P. Yalovets, "The nonlinear dynamics of the interface between media possessing different densities and symmetries," Tech. Phys. Lett. **27**, 20 (2001).
[25] R. L. Holmes, G. Dimonte, B. Frywell, M. L. Gittings, J. W. Grove, M. Schneider, D. H. Sharp *et al.*, "Richtmyer–Meshkov instability growth: experiment, simulation and theory," J. Fluid Mech. **389**, 55 (1999).
[26] D. Ofer, D. Shvarts, Z. Zinamon, and S. Orszag, "Mode coupling in nonlinear Rayleigh–Taylor instability," Phys. Fluids B **4**, 3549 (1992).
[27] C. Hirsch, *Numerical Computation of Internal and External Flows* (Wiley, New York, 1988).
[28] G. Dimonte and B. Remington, "Richtmyer–Meshkov experiments on the Nova laser at high compression," Phys. Rev. Lett. **70**, 1806 (1993).
[29] G. Dimonte, C. E. Frerking, M. Schneider, and B. Remington, "Richtmyer–Meskov instability with strong radiatively driven shocks," Phys. Plasmas **3**, 614 (1996).